Characterization of competing distortions in YFe_2O_4

J. Blasco,[1,*] S. Lafuerza,[2] J. García,[1] G. Subías,[1] V. Cuartero,[2] J. L. García-Muñoz,[3] C. Popescu,[4] and I. Peral[5]

[1]*Instituto de Ciencia de Materiales de Aragón, Departamento de Física de la Materia Condensada, Consejo Superior de Investigaciones Científicas (CSIC)-–Universidad de Zaragoza, E-50009 Zaragoza, Spain*

[2]*ESRF-The European Synchrotron Radiation Facility, 71, Avenue des Martyrs, F-38042 Grenoble Cedex, France*

[3]*Institut de Ciència de Materials de Barcelona, ICMAB-CSIC, Campus univ. de Bellaterra, E-08193 Bellaterra, Spain*

[4]*CELLS-ALBA Synchrotron Light Facility, Ctra. BP1413 km 3.3, E-08290 Cerdanyola del Vallès, Barcelona, Spain*

[5]*Physique et Materiaux, Faculté des Sciences, de la Technologie et de la Communication, Campus Limpertsberg, Université du Luxembourg, L-1511 Luxembourg*

(Received 29 December 2015; revised manuscript received 19 February 2016; published 25 May 2016)

We report the structural changes of three $YFe_2O_{4-\delta}$ ($\delta < 0.1$) specimens using high resolution synchrotron x-ray powder diffraction between 80 and 300 K. All samples adopt a rhombohedral cell at room temperature (space group $R\bar{3}m$). This cell becomes unstable for the three samples on cooling, and the oxygen-poor specimen ($\delta \sim 0.1$) shows a single transition at 240 K. The nearly stoichiometric ($\delta \leqslant 0.03$) compounds exhibit two structural transitions with decreasing temperature at about 240 and 200 K. Each transition is revealed by an anomaly in the heat capacity measurements and a jump in the electric resistivity. Below 240 K, a strong splitting of some diffraction peaks is accompanied by the occurrence of superstructure peaks that follow the propagation vector $\mathbf{k} = (1/7, -2/7, 9/7)$. The cell symmetry is then triclinic, and the structural transition is characterized by an expansion of the c axis coupled to a contraction of the other two lattice parameters. There are 49 nonequivalent sites for Fe atoms with a maximum charge disproportionation of $\sim 0.5\,e^-$. Upon cooling at 200 K, the previous superstructure peaks begin to vanish, and finally they are replaced by a new set of superstructure peaks following the propagation vector $\mathbf{k} = (1/4, 1/2, 1/4)$ with respect to the rhombohedral cell. The transition is also reflected in sudden changes in the lattice parameters that seem to smooth the changes observed in the previous transition. The new cell is also triclinic, and there are 48 nonequivalent Fe sites with a maximum charge disproportionation of $\sim 0.7\,e^-$. Both phases coexist in a wide temperature range because this second transition is not completed at 80 K. A symmetry mode analysis indicates a complicated pattern for the charge distribution in the Fe sublattice of both distorted structures but clearly discard any bimodal distribution of only two types of Fe cations. Therefore, the sharp jumps in the electric resistivity at the phase transitions are clearly correlated with two different structural changes. Finally, the oxygen stoichiometry seems to be a key factor in the stabilization of the different distorted structures.

DOI: 10.1103/PhysRevB.93.184110

I. INTRODUCTION

In recent years, the study of RFe_2O_4 compounds (R = Y or heavy rare earth) has experienced great interest due to their potential multiferroic properties [1–4]. The crystal symmetry of these compounds belongs to the rhombohedral system with space group $R\bar{3}m$, although it is usually described in the hexagonal setting. The undistorted hexagonal structure of these compounds at high temperature can be viewed as a stack of alternating triangular R-O single layer and triangular Fe-O double layers (hereafter denoted as Fe bilayer) along the c axis. Early works suggested that these compounds undergo a charge ordering (CO) transition from a mixed valence $Fe^{2.5+}$ in the rhombohedral phase into an even mixture of Fe^{2+} and Fe^{3+} ions in a distorted structure on cooling. The triangular iron lattice is detrimental for a checkerboard ordering of both cations [5], and then, CO models with polar bilayers were proposed by considering one of the layers rich in Fe^{2+} and the other rich in Fe^{3+}. This special CO allows a possible ferroelectric ordering between consecutive Fe bilayers that is added to the ferrimagnetic order observed in these materials [1,6]. However, bulk ferroelectricity is severely questioned today [7–10], and recent structural studies [11,12] have shown nonpolar CO in $LuFe_2O_4$ and even the lack of only two ionic species [13–15].

Our previous structural study [15] of RFe_2O_4 (R = Tm, Yb, and Lu) ferrites revealed that the rhombohedral structure is quite strained with R atoms overbonded, whereas Fe ones are underbonded; this type of strain increases with increasing the R size. The YFe_2O_4 is a key case because it is the compound with the biggest R^{3+} cation belonging to this family. Second, this is the material exhibiting the widest oxygen nonstoichiometry range, being the physical properties very sensitive to it [16]. Finally, this is the only member in this family of compounds showing two sharp anomalies in the electric resistivity at the CO transition in analogy to other systems with similar transitions such as magnetite or nickelates [17–20]. Nevertheless, the determination of the distorted YFe_2O_4 structure below the CO transition has remained incomplete as it is a very challenging task. Different studies have been performed using mainly powdered samples due to the difficulty in growing single crystals with the accurate stoichiometry. Pioneering works detected two structural transitions in stoichiometric YFe_2O_4 and reported a transition from the hexagonal lattice to monoclinic at 230 K and then to

*Corresponding author: Instituto de Ciencia de Materiales de Aragón, CSIC-Universidad de Zaragoza, Pedro Cerbuna 12, 50009 Zaragoza (Spain); jbc@unizar.es

triclinic at 190 K [21]. Subsequent measurements by high-resolution neutron diffraction indicated that the symmetry is triclinic at 225 K and confirmed a different triclinic structure at 80 K, but they could not assign simple indices to magnetic reflections [22]. Neutron diffraction experiments on deficient $YFe_2O_{4-\delta}$ found two-dimensional spin ordering and $(h/3, h/3, l)$ magnetic peaks [23]. Later studies confirmed the low dimensional ordering in nonstoichiometric samples, while stoichiometric specimens showed three-dimensional ordering coupled to a crystal distortion [24]. No details about the distortion type were reported. More recently, electron diffraction experiments have taken over in the study of distorted structures in YFe_2O_4. According to superstructure peaks, the first studies revealed up to four different phases ascribed to four different types of Fe^{2+}-Fe^{3+} orderings [25]. Successive structural transitions were also reported for $YFe_2O_{4-\delta}$, including diffuse scattering along $(1/3, 1/3, l)$ and superstructure reflections indexed as $(1/3, 1/3, 1/2)$, $(-2/7, 1/7, 9/7)$, and $(-1/14, 2/7, 1/14)$ [26,27]. Recently, stoichiometric single crystals have been grown by the floating zone method. Its study by x-ray diffraction revealed diffuse scattering in $(1/3, 1/3, l)$ reflections, similar to what was found for $LuFe_2O_4$ above the CO transition. However, defined superstructure diffraction peaks following the propagation vector $k = (1/4,1/4,3/4)$ were found at low temperature in these YFe_2O_4 single crystals [28]. The complicated CO pattern and the large amount of twin components prevented a deep structural analysis.

In the absence of a definitive structure, many superstructure cells for the YFe_2O_4 sample at low temperature have been proposed so far. However, the number of phases and transitions occurring in this compound remain unclear [21–28]. The present paper is devoted to gaining insights into the possible distortions that appear below the two CO transitions in nearly stoichiometric $YFe_2O_{4-\delta}$ ($\delta \leqslant 0.03$) by using high resolution synchrotron x-ray diffraction. The problems of twinning, extinction, and multiple-scattering effects deeply complicate the single-crystal studies of YFe_2O_4. These problems are less important in powder diffraction measurements, although the peak overlapping with the loss of information is an important disadvantage. This drawback can be overcome by using high resolution synchrotron x-ray diffraction, which allows the collecting of a large amount of sharp reflections, greatly increasing the chance of structural refinement. We have studied three specimens characterized by different macroscopic properties. The structural study was mainly focused on the nearly stoichiometric sample. Our paper confirms the existence of two structural transitions for this compound and the coexistence of two different triclinic phases in a wide temperature range. Moreover, the effect of oxygen stoichiometry on the emergence of distorted phases has also been studied.

II. EXPERIMENTAL SECTION

Preliminary studies have determined that the YFe_2O_4 phase is present in the phase equilibria of the Fe-Fe_2O_3-Y_2O_3 system at 1200 °C but that it is not stable at 1100 °C [29,30].

Our experience using the CO/CO_2 atmosphere, also used for the synthesis of other RFe_2O_4 samples [15], tells us that sample quality is improved by sintering above 1200 °C followed by a fast cooling. The use of either lower temperatures or slower cooling rates results in a significant presence of impurities. The best results were obtained using temperatures between 1240 and 1280 °C; above 1300 °C, partial melting of the pellets was detected. In the present paper, we report on the properties of specimens prepared under these conditions.

The YFe_2O_4 samples were prepared by solid state chemistry method. Stoichiometric amounts of Y_2O_3 and Fe_2O_3 with nominal purities not less than 99.99% were mixed, ground, and heated at 1200 °C in a CO/CO_2 (2/3) atmosphere for 12 h. The powder was reground, pressed into pellets, and sintered in the same atmosphere for another 12 h at 1260 °C (specimen A), 1280 °C (specimen B), and 1300 °C (specimen C). The sintering was followed by a fast cooling (10 °C/min) to avoid phase decomposition. X-ray diffraction patterns were collected at room temperature using a Rigaku D/Max-B instrument with a copper rotating anode to control the quality of the samples. Specimens A and B were single phase while specimen C showed tiny impurities of Fe_2O_3 and Y_2O_3. The chemical composition of the samples was tested by using the wavelength dispersive x-ray fluorescence spectrometry technique (ADVANT'XP+ model manufactured by ARL). The cationic composition agreed with the nominal one for all samples. Oxygen content of our samples was inferred from macroscopic physical properties.

Synchrotron x-ray diffraction patterns were measured at the MSPD beamline [31] at the Alba synchrotron using the MAD26 detector [32]. The samples were loaded in a borosilicate glass capillary (diameter of 0.5 mm) and kept spinning during data acquisition. A short wavelength, $\lambda = 0.4137$ Å, was selected to reduce absorption. The value of λ was calibrated using standard silicon. The patterns were collected between 80 and 300 K. The standard acquisition time to refine unit cells was about 30 min, but a total acquisition time of 3 h/pattern was used to perform a full structural characterization at selected temperatures.

Diffraction patterns were analyzed by the Rietveld method using the FullProf program [33] with the symmetry-mode analysis. The input file with the basis modes was obtained from the AMPLIMODES program [34] from Bilbao Crystallographic server. AMPLIMODES/SYMMODES and ISODISTORT, the new version of the ISODISPLACE program [35], were used to explore the possible distortions arising from the parent structure of YFe_2O_4.

Differential scanning calorimetry (DSC) was measured using a DSC Q-20 from TA-Instruments with samples sealed in aluminum pans under a nitrogen atmosphere. The scanning rate was 10 K min^{-1}. Magnetic measurements were carried out between 5 and 300 K by using a commercial Quantum Design (SQUID) magnetometer, and electrical dc resistivity measurements were made on rectangular bars cut from the pellets with a typical size of $2 \times 2 \times 9$ mm^3. The conventional four-probe configuration was used, and electrodes were made using silver paint. The software controlling the experimental setup and the data acquisition was developed using LabVIEW. The electrical resistance was measured dynamically by using an Oxford Instruments cryostat in cooling and heating runs at an average speed of 2 K min^{-1}.

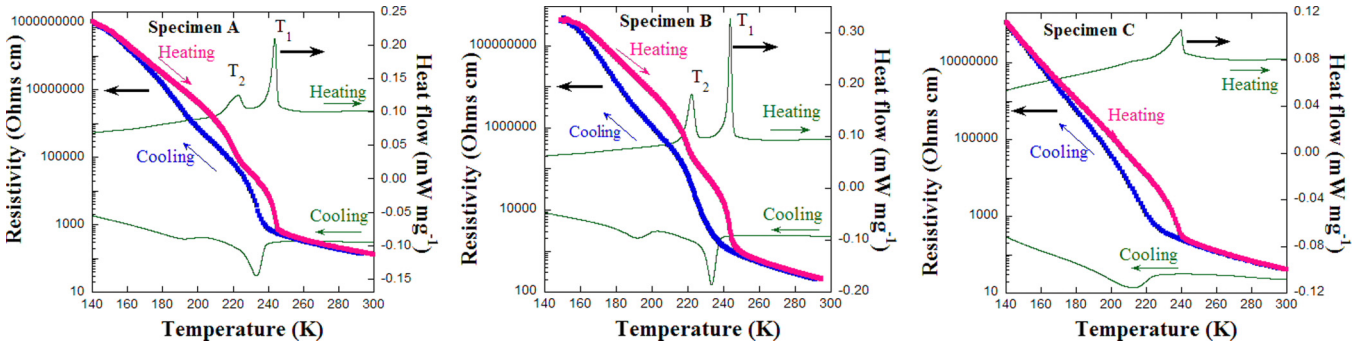

FIG. 1. Comparison of the temperature dependence of DSC and electric resistivity measurements for three specimens of YFe_2O_4 obtained from different sintering conditions. The specimen name is indicated in each plot.

III. RESULTS AND DISCUSSION

A. Physical properties

In order to ensure the quality and oxygen stoichiometry of the three samples, a detailed macroscopic characterization of the physical properties is performed. Figure 1 shows heating and cooling scans of DSC measurements for the three samples, and they are compared to electric resistivity. Two clear peaks are noticeable for specimens A and B in the heat capacity while a single peak is observed for specimen C. The peaks are correlated to phase transitions with sudden changes in the resistivity curves. Specimens A and B show two jumps in the electric resistivity with decreasing temperature while a single jump is observed in specimen C. All transitions show strong hysteresis, suggesting that they are first-order phase transitions. The main difference between specimens A and B concerns the magnitude of the peaks associated with the transitions in the DSC curves. In specimen A, the high temperature peak is at $T_1 = 242\,\mathrm{K}$ while the low temperature peak is at $T_2 = 221\,\mathrm{K}$. There is a shift of about 10 K for T_1 between heating and cooling curves, while this hysteresis is 30 K for T_2. The phase-transition enthalpies, $\Delta H = \int \Delta Cp(T)dT$, are 1168 and 634 $\mathrm{J\,mol^{-1}}$ for the high and low temperature transitions, respectively. The total change in the entropy is 4.82 $\mathrm{J\,mol^{-1}\,K^{-1}}$ for the high temperature transition and 2.9 $\mathrm{J\,mol^{-1}\,K^{-1}}$ for the low temperature one. These values are approximately $0.58R$ and $0.34R$, with R being the gas constant, and the entropy content for the low temperature transition is about 59% of the high temperature transition. In the case of specimen B, the peaks are located at $T_1 = 242.2\,\mathrm{K}$ and at $T_2 = 221.4\,\mathrm{K}$, very close to the peaks observed in specimen A. The hysteresis ranges are also quite similar, but the DSC peaks are more intense in specimen B. Then, the phase transition enthalpies are 1538 and 1037 $\mathrm{J\,mol^{-1}}$ for high and low temperature transitions, respectively. The associated entropies are 6.35 $(0.76R)$ and 4.68 $(0.56R)$ $\mathrm{J\,mol^{-1}\,K^{-1}}$, i.e., the entropy content for the low temperature transition is about 74% of the one for the high temperature transition, significantly higher than the ratio observed for specimen A. Finally, specimen C shows a single peak with $\Delta H = 561\,\mathrm{J\,mol^{-1}}$ and $\Delta S = 2.36\,\mathrm{J\,mol^{-1}\,K^{-1}}$. These smaller values may be related to an increase of defects for this specimen.

Figure 2 shows the dc magnetization measurements of the three specimens collected in heating scans. Zero field cooled (ZFC) and field cooled (FC) conditions were probed with an external field of 4 kOe. Specimens A and B exhibit a similar behavior with a small magnetic irreversibility at low temperatures. In both cases, the magnetization shows a peak at about 245 K, indicating the development of long range magnetic ordering [22,28]. This temperature coincides with the one for the high temperature peak in the DSC scan (T_1). Surprisingly, the FC branch has a lower magnetization than the ZFC branch at low temperature in these specimens. Both branches intersect at about 145 K (specimen A) and 115 K (specimen B), and the magnetic irreversibility is significantly smaller for specimen B. The comparison to previous reports [16] on $YFe_2O_{4-\delta}$ suggests a slight oxygen deficiency of $\delta \sim 0.03$ for both specimens.

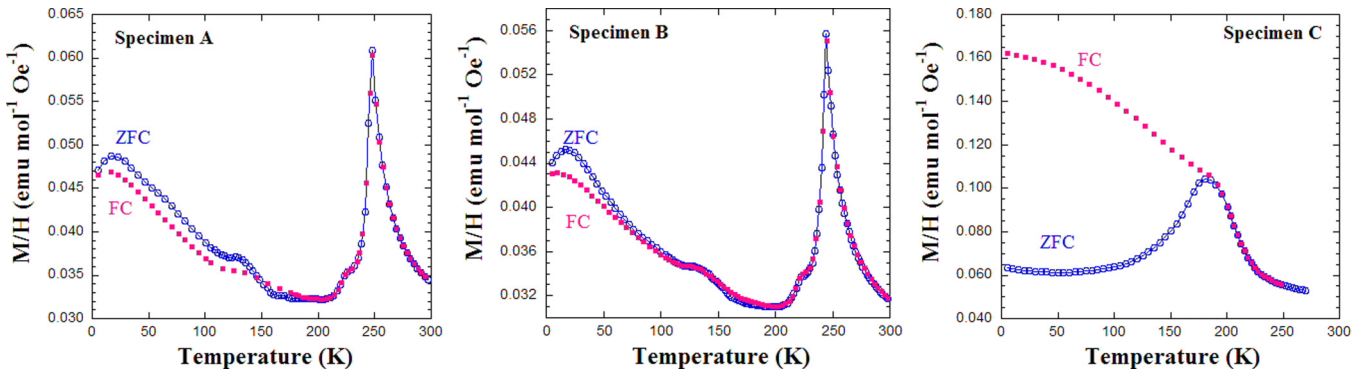

FIG. 2. Magnetization of the three specimens of YFe_2O_4 indicated in the plots. The measurements were made by heating with an external dc field of 4 KOe.

Regarding specimen C, its magnetization is the largest of these samples. The ZFC measurement shows a peak at about 185 K, and a strong magnetic irreversibility is observed below this peak as the FC branch behaves as a conventional ferrimagnet. According to Ref. [16], this behavior is typical of samples with an oxygen deficiency of $\delta \sim 0.095$. In this case, the magnetic transition temperature does not match with the DSC peak, suggesting that the entropy content of the latter only arises from the electronic localization of the semiconductor-insulator transition.

According to Ref. [17], our specimens A and B with two electric transitions behave as oxygen stoichiometric compounds ($\delta = 0$), whereas their magnetic properties [16] are in agreement with $\delta < 0.03$. Therefore, both properties specify nominal oxygen content very close to the stoichiometric sample. Conversely, specimen C, which shows a single phase transition, exhibits significant oxygen deficiency. As specimen B is the one showing the transitions with the highest entropy content, our structural study will be mainly focused on this sample, with occasional references to the other two specimens to highlight the most significant differences.

B. Crystal structure at room temperature

The x-ray diffraction patterns of YFe_2O_4 compounds at room temperature agree with a single-phase rhombohedral structure for specimen B, while specimen A shows tiny impurities of $YFeO_3$ (0.9 wt%) and FeO (0.4 wt%) and specimen C shows the highest amount of these impurities (2.8 wt% of $YFeO_3$ and 1.3 wt% of FeO). This result suggests that the optimum sintering temperature is about 1280 °C to obtain single phases using the abovementioned atmosphere.

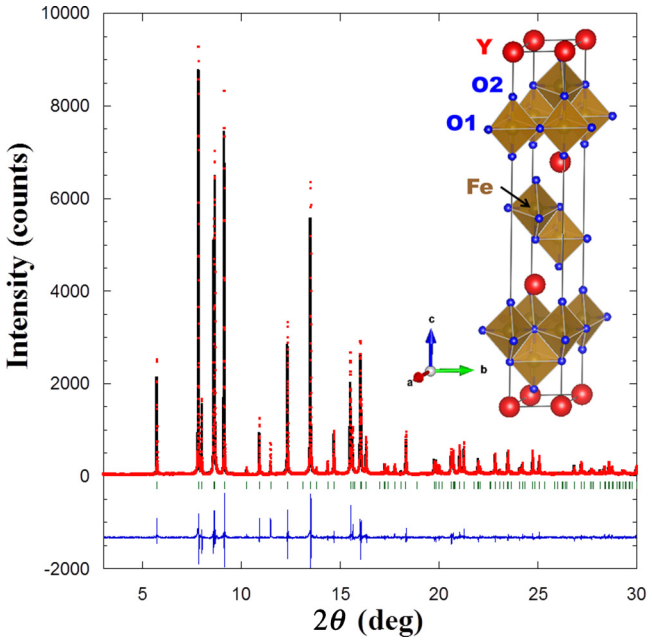

FIG. 3. Rietveld refinement of YFe_2O_4 at 290 K. Points and continuous line refer to experimental and calculated patterns, respectively. The difference is plot at the bottom with the allowed reflections.

TABLE I. Refined structural parameters (lattice, fractional coordinates, and temperature factors) and reliability factors at 290 K for YFe_2O_4. The space group is $R\bar{3}m$ in the hexagonal setting, and the Wyckoff positions are indicated for each atom.

a (Å)	3.51621(1)
c (Å)	24.7878(1)
Vol. (Å^3)	265.410(2)
Y (3*a*):	
B (Å^2)	1.28(1)
Fe (6*c*): z	0.21418(3)
B (Å^2)	1.41(3)
O1 (6*c*): z	0.1268(1)
B (Å^2)	2.7(1)
O2 (6*c*): z	0.2939(1)
B (Å^2)	0.87(8)
R_p (%)	
R_{Bragg} (%)	4.7
R_F (%)	4.4

Figure 3 shows the x-ray pattern of specimen B at 290 K. The pattern was refined with the space group $R\bar{3}m$ using the hexagonal setting, and the results concur with previous reports [21]. The structural refined parameters are summarized in Table I; hereafter, we denote this phase as R (rhombohedral). Among these data, the high value of the temperature factors for some atoms, especially O1, which may be associated with a strong dynamic disorder, is noteworthy. An estimate of the atomic valence has been obtained by the bond valence sums (BVS) method [36] yielding the values of +3.17, +2.30, −1.73, and −2.15 for Y, Fe, O1, and O2 atoms, respectively. These results imply that Y and O2 are overbonded while Fe and O1 are underbonded, and they are likely related to the big size of Y^{3+} cations to be placed in this rhombohedral lattice. The size mismatch results in a compressible strain for the Y-O2 sublattice and a tensile strain for the Fe-O1 one. Regarding Fe atoms, the nominal mixed valence value of +2.5 is significantly reduced by the structural constrain of the R phase.

C. Phase transitions with decreasing temperature

Upon decreasing temperature, strong changes are observed in the x-ray patterns characterized by the splitting of a significant number of diffraction peaks and the appearance of new superstructure reflections. The measurements were performed in two ways: either cooling down to 80 K and then collecting patterns at selected temperatures when heating the sample or cooling from room temperature down to 80 K and measuring at the same points. We have identified two structural transitions, and the main changes observed in the x-ray patterns occur at the temperatures where peaks are visible in the DSC curves. The structural changes are best observed in the patterns obtained by the second measurement method (cooling from room temperature) as the temperature gap between both transitions is higher due to the experimental hysteresis (see Fig. 1). The first structural change is perceptible at about 240 K, and the observed splitting indicates that the lattice is no longer rhombohedral but triclinic. This structure is denoted hereafter

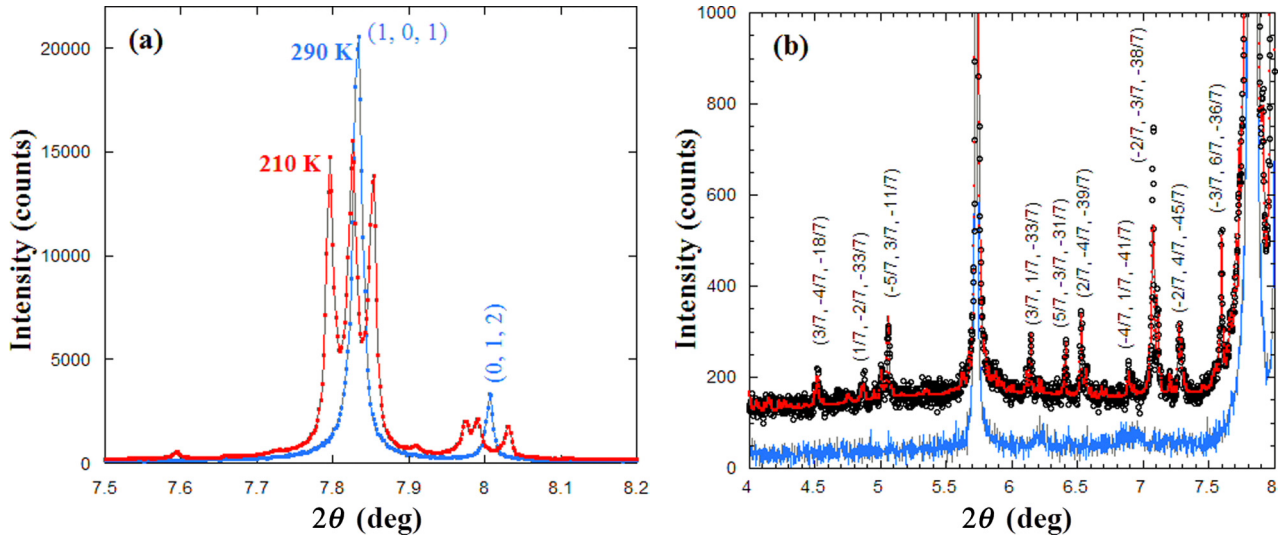

FIG. 4. (a) Comparison of selected x-ray patterns of YFe_2O_4 collected at 290 and at 210 K. (b) Detail of the x ray (points) collected at 210 K showing the occurrence of superstructure peaks with the indexation related to the high temperature rhombohedral phase. The line stands for the theoretical refinement using the model indicated in the text. Bottom (blue line online): Detail of the x-ray pattern collected at 290 K. It was shifted downward for the sake of comparison.

as high-temperature triclinic (HTT). The second structural transition is observed at about 180 K on cooling. This is characterized by the vanishing of some superstructure peaks and the occurrence of new ones together with a strong change of the lattice parameters. The lattice remains triclinic and is denoted as low-temperature triclinic (LTT). The main features of both distorted structures are shown below. Hereafter, the superstructure peaks are indexed in the frame of the hexagonal setting of the room temperature cell.

1. *Crystal structure at 210 K*

Figure 4 compares the x-ray patterns collected at 290 and 210 K. The strong splitting of some diffraction peaks and the occurrence of new satellites are discernible. We have used ISODISTORT software to explore possible distortions that are able to produce transitions from the parent R-cell to a triclinic cell with $P\bar{1}$ space group. The peak splitting can be accounted for by a wide set of triclinic cells; some of them are summarized in the Table II. The simplest triclinic cell (primitive in fact) is obtained by the condensation of modes belonging to the irreducible representation (Irrep) GM3+. Obviously, this cell is unable to explain the new superstructure peaks, but refinements with $R_{Bragg} \sim 8.6\%$ can be obtained indicating the little weight that superstructure peaks have in the global refinement of this pattern. The second cell in Table II can be considered as the triclinic cell equivalent to the distortion found in $LuFe_2O_4$ (monoclinic in that case) [11,15]. In both cases, the condensing modes responsible for the transition belong to Y1 and Y2 Irreps. This distortion leads to superstructure peaks indexed as $(h/3, k/3, l/2)$ that are absent in the x-ray pattern of YFe_2O_4, emphasizing the different distorted structures for YFe_2O_4 and $LuFe_2O_4$.

The third cell described in Table II arises from condensing modes belonging to the Irrep LD with (0, 0, 1) k-point. This is the cell reported in Ref. [21]; the lattice parameters are similar to the parent hexagonal lattice with the consequent changes in the lattice, but it does not explain the superstructure peaks. Given the great similarity between this triclinic cell and the R one, we have made use of it to index the new satellites and have found that all satellites can be indexed as $(h/7, k/7, l/7)$, as indicated in Fig. 4(b). This result resembles the solution found in a previous electron diffraction study [27] where the satellites can be indexed by the propagation

TABLE II. Selected distorted structures yielding triclinic structures from a rhombohedral cell by condensation of modes belonging to the indicated Irreps and k-points.

Primary mode (k-point)	Transformation matrix	Refined cell (Å and deg)
$GM3+$ (0, 0, 0)	$\boldsymbol{a}_t = (1,0,0)$	$a = 3.5332, \alpha = 78.366$
	$\boldsymbol{b}_t = (1,1,0)$	$b = 3.5102, \beta = 78.514$
	$\boldsymbol{c}_t = (2/3,1/3,1/3)$	$c = 8.4820, \gamma = 59.903$
$Y1 + Y2$ $(a, a, 3/2)$	$\boldsymbol{a}_t = (1, -1,0)$	$a = 6.102\,700, \alpha = 90.222$
$a = 1/3$	$\boldsymbol{b}_t = (-3, -3,0)$	$b = 10.549\,563, \beta = 97.527$
	$\boldsymbol{c}_t = (-1/3,1/3, -2/3)$	$c = 16.648\,823, \gamma = 89.570$
LD (0, 0, g)	$\boldsymbol{a}_t = (1,1,0)$	$a = 3.533\,25, \alpha = 90.179$
$g = 1$	$\boldsymbol{b}_t = (-1,0,0)$	$b = 3.516\,62, \beta = 89.476$
	$\boldsymbol{c}_t = (0,0,1)$	$c = 24.757\,77, \gamma = 120.275$

TABLE III. Selected triclinic distortion arising from a rhombohedral cell by combination of SM and LD Irreps.

Primary mode	Transformation matrix	Undistorted cell (Å and deg)
SM1 (or SM2) + LD3	$\mathbf{a_t} = (2, -1, 0)$	$a = 6.093\,53$, $\alpha = 89.517$
	$\mathbf{b_t} = (-1, 3, 0)$	$b = 12.684\,69$, $\beta = 87.991$
	$\mathbf{c_t} = (2/3, 1/3, 7/3)$	$c = 57.927\,72$, $\gamma = 76.102$
SM1 (or SM2) + LD1	$\mathbf{a_t} = (0, 7, 0)$	$a = 24.626\,70$, $\alpha = 78.079$
	$\mathbf{b_t} = (7, 7, 0)$	$b = 24.626\,70$, $\beta = 78.079$
	$\mathbf{c_t} = (7/3, 14/3, -7/3)$	$c = 59.612\,53$, $\gamma = 60.00$

vector $\mathbf{k} = (1/7, -2/7, 9/7)$. Therefore, we have explored distorted structures coming from the mode condensation belonging to the combination of two Irreps: SM(a, $-2a$,0) and LD(0, 0, g) with $a = 1/7$ and $g = 9/7$. ISODISTORT yields two possible solutions with $P\bar{1}$ space group; they are indicated in Table III. Both solutions refer to big cells with a large amount of free parameters. The only solution accessible to our software package was the first one, and we have tested the reliability of this solution. In this unit cell, there are 25 Y, 49 Fe, and 98 O; this leads to a total of 513 coordinates to be refined, which is at the limit of current software packages. There are a total of 24 892 reflections in our pattern, but FullProf calculated 1102 useful reflections taking into account resolution and overlapping. This implies that about 275 parameters should be refined in order to avoid overparameterization. Therefore, the refinement was performed step by step and by using several constrains and approximations. First, we have refined only three temperature factors (B_{iso}): one for each type of atom. Second, we have refined each family of modes separately, and those modes giving rise to reflections absent in the patterns were neglected (the amplitudes were then fixed to zero). This was the case for all SM and LD1 modes, for example. We realized that two families of modes can account for all superstructure reflections. They belong to the global points GP(2/7, 2/7, 3/7) and GP(1/7, 3/7, 1/7). Thus, we started the refinement step by step beginning with the refinement of GM modes. In this point, the refinement could account for the peak splitting but not for superstructure peaks. Then, we added each family of modes, one by one, checking the results after each step. The modes whose standard deviation systematically overcomes the value of its amplitude were discarded. In the end, our model comprises 72 mode amplitudes, and in any case we never refined more than 150 amplitudes at once. The parameters of the refined cell are $a = 6.074\,01(4)$ Å, $b = 12.740\,28(9)$ Å, $c = 57.809\,24(39)$ Å, $\alpha = 90.0028°(2)$, $\beta = 87.8954°(3)$, and $\gamma = 76.0896°(2)$, resulting in a cell volume of 43 339.24(5) Å^3. The refinement can be seen in Fig. 5, and detail of the superstructure peaks can be seen in Fig. 4(b). The refined fractional coordinates and mode decomposition are summarized in the Supplemental Material [37], and the reliability factors of the fit are $R_{Bragg} = 5.4\%$ and $R_F = 3.7\%$.

Regarding the Fe sublattice, the most important numbers are as follows: There are 49 nonequivalent sites, and the valences calculated by the BVS method ranges between 2.15 and 2.67 with a mean value of 2.37(14). Bearing in mind the accuracy of the BVS method (estimated in our system about 0.15 valence units), these results can be viewed as a continuous distribution of formal valences between the two mentioned limits. Compared to the parent rhombohedral cell, this implies an increase of the Fe mean valence with the consequent relief of the tensile strain. Figure 6 shows the HTT cell and its relationship with the parent cell. The structure can be viewed as a stacking of seven Fe bilayers along the triclinic c axis. These bilayers are related by a symmetry center in the middle of the unit cell, preventing the formation of ferroelectric ordering. In essence, charge segregation compatible with antiferroelectric arrangements is possible; however, the charge modulation along the c axis is very small, and the biggest difference between neighbor bilayers calculated by the BVS method is only 0.04 valence units. Something similar happens when one looks at the individual bilayers. The charge difference between the individual layers composing a bilayer is negligible in most of them and is always below the BVS accuracy.

2. *Crystal structure at 80 K*

On cooling the sample below 180 K, new changes are noticeable in the x-ray patterns. New peaks begin to appear while the superstructure peaks belonging to the HTT phase vanish. At lower temperatures, some new peaks become so intense that they clearly belong to a new phase. Simultaneously,

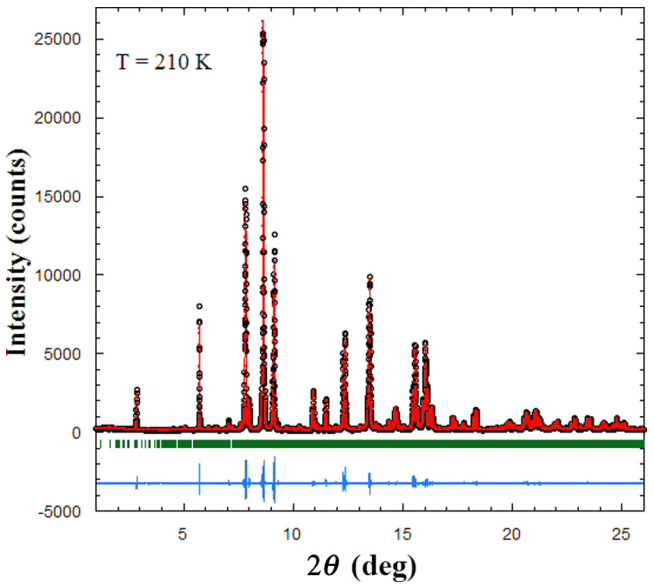

FIG. 5. Rietveld refinement of YFe_2O_4 at 210 K cooling from room temperature. Point and red line (online) refers to experimental pattern and fit. Bars below indicate the allowed reflections, and the blue line at the bottom shows the difference between experimental and calculated pattern.

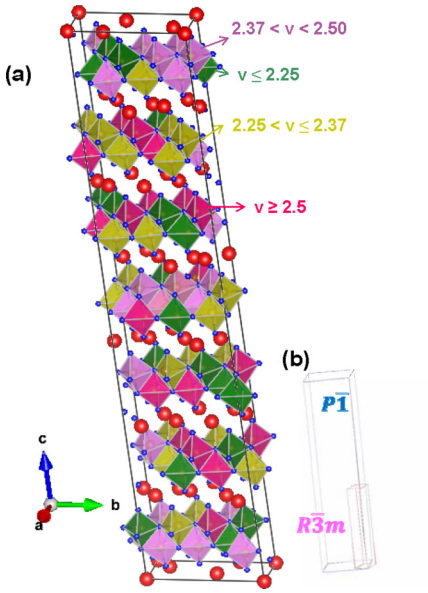

FIG. 6. (a) Crystal structure of YFe_2O_4 at 210 K (HTT phase). Big and small balls represent Y and O, respectively. Bipyramids have been colored (online) according to the valence ranges indicated in the plot. (b) Relationship between crystal lattices observed for the room temperature structure (rhombohedral, $R\bar{3}m$) and HTT phase (triclinic, $P\bar{1}$).

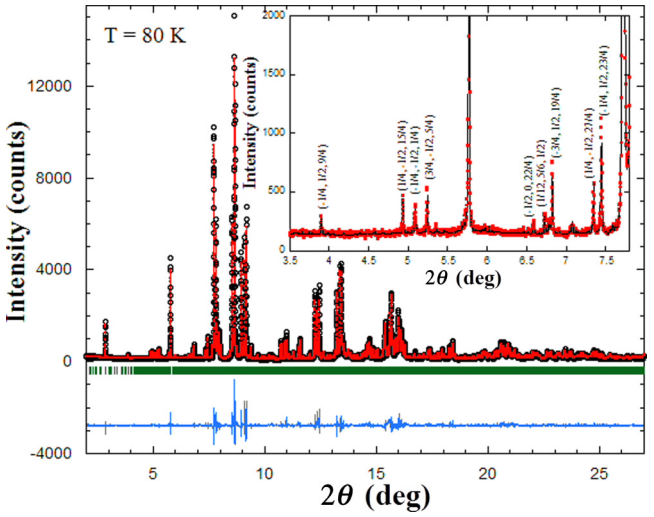

FIG. 7. Rietveld refinement of YFe_2O_4 at 80 K. Point and red line (online) refers to experimental pattern and fit. Bars below indicate the allowed reflections, and the blue line at the bottom shows the difference between experimental and calculated pattern. Inset: Detail of the x-ray pattern showing the main superstructure peaks and the indexation respect to the R phase.

the intensity of the main peaks belonging to the HTT phase decrease and also become wider. This suggests a collapse of the HTT phase with decreasing temperature. In any case, the signature of the HTT phase is still present in the pattern collected at 80 K, indicating that the transformation is not completed. A pattern with high statistics was acquired at this temperature with the aim of performing a full structural refinement. However, the refinement with two large triclinic cells was proved to be impossible, so two approximations were assumed. As superstructure peaks coming from the HTT phase are not visible in the pattern collected at 80 K, this phase was modeled by the simplest primitive triclinic cell (corresponding to the model GM3+ in Table II). This approximation reduces the number of free parameters, but it is not enough to stabilize the structural refinements. The second approximation was to refine the HTT phase only and then to subtract this contribution to the experimental pattern, as indicated in Fig. S1 in the Supplemental Material [37]. With this procedure, we obtained a pattern containing only the structural information from the LTT phase; this was used to refine its crystal structure.

This pattern can be refined using similar models to the ones indicated in Table II. Together with the main peaks, a set of superstructure peaks are clearly perceptible. The superstructure peaks can be indexed as $(h/4,\ k/2,\ l/4)$ by using a triclinic cell with lattice parameters similar to the undistorted R phase (matching model LD in Table II). Making use of ISODISTORT, the simplest cells able to account for these peaks are summarized in Table IV. There are four possible solutions in which the transformation matrix relating the LTT phase with the R lattice is $\mathbf{a_t} = (-2, -1, 0)$, $\mathbf{b_t} = (0, -6, 0)$, and $\mathbf{c_t} = (2/3, 1/3, 4/3)$. Pattern matching using this cell confirmed that it is possible to account for all peaks presented in the diffraction pattern, as can be seen in the inset of Fig. 7. The structural refinements highlighted two families of superstructure peaks. The majority of these satellites can be explained by the condensation of phonons belonging to the Irrep GP $(1/4, 1/4, 3/4)$, but there are a number of new peaks such as the ones indexed as $(1/2, -1, 8)$,

TABLE IV. Four different possible final structures resulting from the same transformation matrix but applying a different origin shift. Main Irreps with active modes are given. All four structures present five Global Points each, with identical k-points (shown in the Supplemental Material [37]) but different directions depending on the origin taken.

Transformation matrix	Origin	Irreps with active modes
$\mathbf{a_t} = (-2, -1, 0)$	(0, 0, 0)	GM1+; GM3+; LD1; LD3; SM1; and SM2 (5 k-points); F1+; F2+; L1+; L2+; T1+; T3+; Y1; and Y2 (5 k-points); C1; C2; GP (5 k-points)
$\mathbf{b_t} = (0, -6, 0)$	(0, 0, ½)	GM1+; GM3+; LD1; LD3; SM1; and SM2 (5 k-points); F1+; F2+; L1-; L2-; T2-; T3-; Y1; and Y2 (5 k-points); C1; C2; GP1 (5 k-points)
$\mathbf{c_t} = (2/3, 1/3, 4/3)$	(1/6, −8/3, 1/3)	GM1+; GM3+; LD1; LD3; SM1; and SM2 (5 k-points); F1-; F2-; L1-; L2-; T1+; T3+; Y1; and Y2 (5 k-points); C1; C2; GP1 (5 k-points)
	(−1/6, −17/6, 1/6)	GM1+; GM3+; LD1; LD3; SM1; and SM2 (5 k-points); F1-, F2-; L1+; L2+; T2-; T3-; Y1; and Y2 (5 k-points); C1; C2; GP1 (5 k-points)

TABLE V. Summary of the mode decomposition for the constrained refinement of the LTT phase.

K-vector	Irrep	Direction	Isotropy subgroup	Dimension	Amplitude (Å)
(0, 0, 0)	GM1+	(a)	$R3m$	3	0.99(4)
(0, 0, 0)	GM3+	(a, b)	P-1	6	1.27(5)
(−1/2,1/2,1/2)	L1−	(0, 0, a)	C2/c	4	1.52(2)
(−1/2,1/2,1/2)	L2−	(0, 0, a)	$C2/m$	8	0.58(5)
(1/4,1/4,3/4)	GP3	(0, 0, a, 0, 0, b, 0, 0, a, 0, 0, −b)	P-1	42	3.01(7)

(−1/2, 0, 5), and (1/2, −1, 3) that can be explained only by the condensation of phonons belonging to Irreps L1- or L2-. This result limits the possible solutions to the second and third models of Table IV. We have performed refinements with the two models; the best result was obtained with the second model, although the limit of free parameters in the refinements does not give full confidence to this choice. In the Supplemental Material [37] there is a summary of the mode decomposition of active modes in a transition from R phase into the LTT one. In our best model, the unit cell contains 24 atoms of Y, 48 of Fe, and 96 of O, yielding a total of 504 fractional coordinates (or mode amplitudes) to be refined. In the pattern, there are a total of 23 403 reflections, of which only 959 can be considered effective reflections due to overlapping. We have proceeded in a similar way to the one used previously to analyze the HTT phase, and finally we have limited the number of free parameters to the modes indicated in Table V for a total of 60 modes amplitudes. In addition, we have refined three B_{iso}, one for each atom type. This refinement yields the following unit cell: $a = 6.102\,20(3)$ Å, $b = 21.518\,06(11)$ Å, $c = 32.863\,62(16)$ Å, $\alpha = 91.1758°(3)$, $\beta = 94.0169°(3)$, $\gamma = 89.8103°(3)$, with reliability factors $R_{Bragg} = 6.6\%$ and $R_F = 3.8\%$. The refinement is shown in Fig. 7, and the fractional coordinates are summarized in the Supplemental Material [37], while Table V shows the results of the structural refinement as a conventional superstructure of the high temperature hexagonal phase when decomposed in Irrep distortions. A distortion with symmetry given by the Irrep GP with a wave vector (1/4,1/4,3/4) of the Brillouin zone is dominant. Secondary modes belong to the Irreps GM3+ and L-1. The addition of more modes from other Irreps (not included in Table V) did not significantly improve the fit and resulted in no physical values for some interatomic distances. However, we have not refined over 200 modes at once to avoid overparameterization, so one cannot discard further improvement with an accurate choice of additional modes. This could amend the excessive temperature factor of O atoms deduced from our model.

In the LTT phase, there are 48 nonequivalent sites for Fe atoms and valences calculated in the range between 1.96 and 2.72 with a mean value of 2.41(25). In comparison with the preceding phases, the Fe mean valence continues increasing with decreasing temperature and approaches the nominal value of +2.5. Figure 8 exhibits the LTT cell. It can be seen as a stacking of four Fe bilayers along the c axis. They are related by pairs as a symmetry center lies in the middle of the central bilayer, and accordingly it is also inconsistent with any charge segregation yielding ferroelectric ordering. The charge difference is very small between consecutive bilayers ($\leqslant$0.02 valence units) and negligible between the layers composing a bilayer.

D. Phase composition as a function of temperature for the three specimens

In order to quantify the ratios of the two phases (HTT and LTT), we have attempted to refine the original pattern at 80 K with both HTT and LTT phases. The high number of parameters precludes such a refinement, so the HTT phase was approximated to the primitive triclinic cell (GM3+ model in Table II) as superstructure peaks arising from this phase are not visible in the x-ray pattern. The refinement was unstable, so in the end we have refined only scale factors, lattice parameters, and profile factors, keeping fixed the mode amplitudes (as refined in the previous section). The fit is surprisingly good at 80 K, as seen in the Supplemental Material [37] (R_{Bragg} is 4.97% and 2.95% for LTT and HTT phases, respectively), and this procedure allowed us the quantification at different temperatures. The results of this quantification are summarized for the three specimens in Fig. 9. The phase composition is dependent on the specimen, suggesting a significant role of the defects in the stabilization of the different distorted phases. The

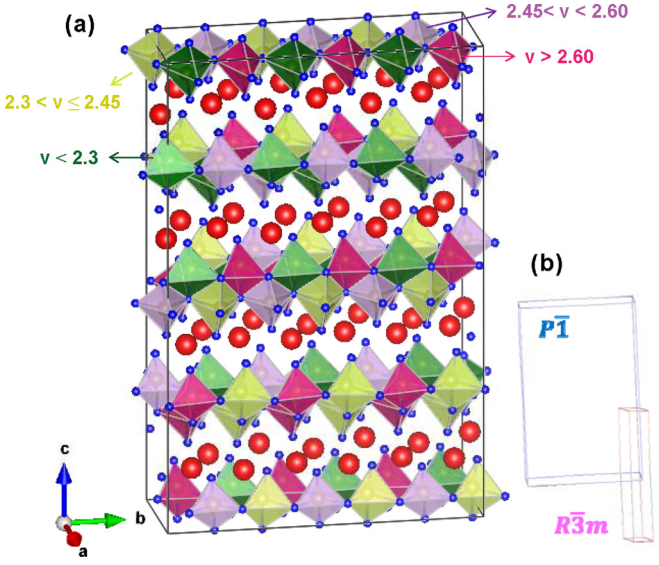

FIG. 8. (a) Crystal structure of YFe_2O_4 at 80 K (LTT phase). Big and small balls represent Y and O, respectively. Bipyramids have been colored (online) according to the valence ranges indicated in the plot. (b) Relationship between crystal lattices observed for the room temperature structure R (rhombohedral, $R\bar{3}m$) and LTT phase (triclinic, $P\bar{1}$).

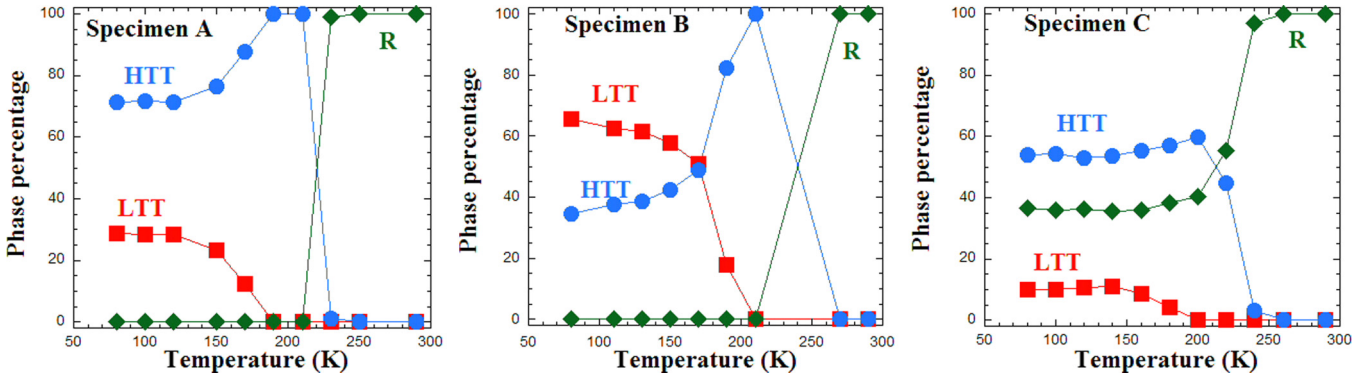

FIG. 9. Temperature dependence for the amount of the different crystal phases presented in the three specimens of YFe_2O_4 obtained by refinement of the x-ray patterns.

LTT phase is the majority in specimen B at 80 K. However, the transition is not complete, and the temperature dependence gives signs of a balance between LTT and HTT phases. Specimen A shows similar transitions with the occurrence of similar phases (not shown here). However, the main phase at 80 K is the HTT one in this case. Here, the equilibrium between both phases is even more evident. The different LTT/HTT ratio at low temperature for these specimens may account for the different entropy content in the transition at $T_2 \sim 221$ K (see Fig. 1). Finally, the most defective sample, specimen C, shows incomplete phase transitions, and the R phase is still present at 80 K. The LTT phase is the minority in the mixture at 80 K, and the main peaks from this phase could be mistaken as superstructure peaks of the majority phase.

Focusing again on specimen B, Fig. 10 displays the temperature dependence of the lattice parameters (referred to as the primitive triclinic cell). It can be appreciated that the transition from the R phase to the HTT phase involves a strong expansion of the *c* axis while the *ab* plane is contracted (especially the *b* axis). However, the next transition from the HTT phase to the LTT phase seems to soften the previous distortion, and here we can see a contraction of the *c* axis coupled to an expansion of the *ab* plane.

IV. CONCLUDING REMARKS

The YFe_2O_4 is unique in the family of RFe_2O_4 compounds. The stoichiometric sample undergoes two consecutive phase transitions on cooling that are coupled to strong changes in the electric properties. Our paper has demonstrated that these transitions are associated to two different structural transitions. These two distorted phases coexist at low temperature in our samples, and the ratio depends on synthesis details. Accordingly, some distorted phases (and then phase transitions) may be absent in non-optimized samples with many defects.

We have made evident that there is a large number of nonequivalent Fe sites showing a wide range of formal valences in the two distorted structures. Traditionally, stoichiometric YFe_2O_4 had been regarded as prototype of two-step Verwey transition [38] in comparison to the conventional one-step transition in magnetite. In both cases, the proposed mechanism for the electric transition was a structural transition coupled to a charge disproportionation in the Fe sublattice. The high temperature and more conductive phase was composed by Fe in mixed valence state, whereas the low temperature phase, and insulating, consisted in an ordered pattern of Fe^{2+} and Fe^{3+} cations. Diffraction and spectroscopic studies soon challenged this ionic picture for the Verwey transition [18], and

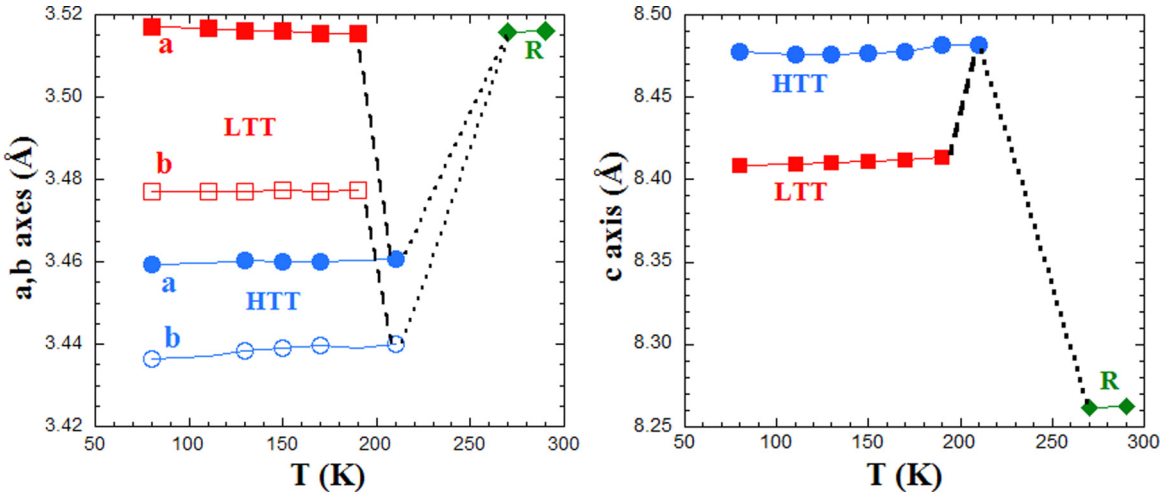

FIG. 10. Temperature dependence of the lattice parameters referred to the primitive triclinic cell for specimen B of YFe_2O_4. The parameter and crystal phase are indicated for each curve.

it was assumed that the disproportionation was not complete and that the insulating phase consisted in a bimodal distribution of $Fe^{2.5+\delta}/Fe^{2.5-\delta}$ cations ($\delta < 0.5$). However, the structure of magnetite below the Verwey transition has been recently solved, revealing the inaccuracy of bimodal distribution of two kinds of Fe atoms to describe the distortions produced in the transition [39]. Something similar happens in YFe_2O_4. None of its two structural transitions can be ascribed to a conventional CO with bimodal distribution of $Fe^{2.5+\delta}/Fe^{2.5-\delta}$ cations. Instead, the transitions seem to be driven by the relaxation of the tensile strain supported by the Fe bilayers due to the large size of Y^{3+} cation. The result is a continuous distribution of $Fe^{\delta i+}$ cations, with δ_i ranging between 2.15 and 2.65 for the HTT phase ($1 \leqslant i \leqslant 49$ nonequivalent Fe sites), whereas the δ_i value is between 2.0 and 2.75 for the LTT one (and $1 \leqslant i \leqslant 48$ nonequivalent Fe sites). The complicated pattern of distortions, which implies the condensation of phonons belonging to several Irreps, suggests the occurrence of competitive interactions or mechanisms for the structural relief that lead to several local minima with small energy barrier among them. This may account for the coexistence of several distorted structures at low temperature. Overall, our analysis also accounts for the results of previous studies. In this way, the changes observed in our patterns are similar to the ones observed in Refs. [21] and [22]. Superstructure peaks observed by electron microscopy [26,27] can be accounted for by the HTT phase, and the changes observed with decreasing temperature [24] might be related to the transition from the HTT into the LTT phase and the subsequent coexistence of both phases. A recent study on a YFe_2O_4 single crystal [28] reports superstructure $(h/4, l/4, k/4)$ peaks at 120 K, in agreement with the results expected for the LTT phase. The same study states that $(h/3, k/3, l)$ peaks are discernible at 10 K, in agreement with the satellites observed for related $LuFe_2O_4$. There was no evidence for another phase transition below 80 K for our samples (DSC scans, for instance). This might be related to small differences between the single crystal and our samples, which may lead to different ground states. However, the similar physical properties and the similar satellite peaks observed at 120 K for both the single crystal and our sample made us consider the possibility of gradual modes activation on cooling. Distortions ascribed to $(1/3, 1/3, 3/2)$ wave vector with symmetry given by the Irreps Y1 and Y2 are allowed for the LTT phase (see complete mode decomposition in the Supplemental Material [37]), and their condensation may increase with decreasing temperature, resulting in new satellites similar to the ones observed in $LuFe_2O_4$ [15].

In conclusion, we have performed a structural analysis of the YFe_2O_4 compound between room temperature and 80 K. We have identified two new distorted structures that can be described to a good approximation by two triclinic cells. In the stoichiometric compound, the transition from the parent rhombohedral structure into the triclinic HTT phase is mainly driven by the condensation of phonons with symmetry given by two global points with wave vector $(2/7, 2/7, 3/7)$ and $(1/7, 3/7, 1/7)$. On cooling, the HTT phase partly collapses and transforms into the LTT phase, also triclinic. This new distortion can be viewed as mainly driven by the condensation of new phonons with symmetry of another global point respect to the undistorted rhombohedral phase and with wave vector $(1/4, 1/4, 3/4)$. The different satellites observed in the x-ray patterns at different temperatures are well explained by these triclinic phases. Finally, oxygen deficiency seems to stabilize the rhombohedral phase that remains in the whole temperature range measured for the least stoichiometric specimen. It is very likely that this is a key factor in the stabilization of a specific distorted structure.

These results have important implications on the physics of this so-called Verwey mixed valence compound. The low temperature distortions lead to a nonpolar crystal structure, and it does not support the occurrence of ferroelectricity. There are 49 and 48 different crystallographic Fe-sites in the HTT and LTT phases, respectively, with a continuous distribution of valences. This result implies that the multiferroicity mechanism driven by a CO of two distinct Fe valences (conventionally, 2+ and 3+) is not operative in this compound as happens in other members of this family of oxides [14,15]. The change in the electric conductivity at the phase transition temperatures cannot be ascribed to the electronic localization at the iron sites either. Instead, it is likely due to gap opening in the valence band by the phonon condensation associated to the observed structural transitions.

Finally, the structural transitions seem to be coupled to the magnetic anomalies observed in the magnetization curves for stoichiometric YFe_2O_4 specimens (see Fig. 2). Our structural study will provide the needed information to discriminate superstructure reflections depending on their origins, structural or magnetic, in further neutron diffraction experiments. It would be desirable in this type of study concerning single crystals to determine whether the magnetic ordering follows the structural changes shown here.

ACKNOWLEDGMENTS

We acknowledge CELLS-ALBA for beam time allocation and the use of Servicio General de Apoyo a la Investigación, Universidad de Zaragoza. We are thankful for financial support from the Spanish Ministerio de Economía y Competitividad (MINECO) (Projects No. MAT2012-38213-C02-1-2 and No. MAT2015-68760-C2-1-2, cofunded by the European Regional Development Fund [ERDF] allocated by the European Union) and Diputación General de Aragón (DGA, project E69).

[1] N. Ikeda, H. Ohsumi, K. Ohwada, K. Ishii, T. Inami, K. Kakurai, Y. Murakami, K. Yoshii, S. Mori, Y. Horibe, and H. Kitô, Nature **436**, 1136 (2005).

[2] M. A. Subramanian, T. He, J. Chen, N. S. Rogado, T. G. Calvarese, and A. W. Sleight, Adv. Mater. **18**, 1737 (2006).

[3] T. Kambe, Y. Fukada, J. Kano, T. Nagata, H. Okazaki, T. Yokoya, S. Wakimoto, K. Kakurai, and N. Ikeda, Phys. Rev. Lett. **110**, 117602 (2013).

[4] C. H. Li, F. Wang, Y. Liu, X. Q. Zhang, Z. H. Cheng, and Y. Sun, Phys. Rev. B **79**, 172412 (2009).

[5] J. van der Brink and D. I. Khomskii, J. Phys.: Condens. Matter **20**, 434217 (2008).
[6] K.-T. Ko, H.-J. Noh, J.-Y. Kim, B.-G. Park, J.-H. Park, A. Tanaka, S. B. Kim, C. L. Zhang, and S.-W. Cheong, Phys. Rev. Lett. **103**, 207202 (2009).
[7] P. Ren, Z. Wang, W. G. Zhu, H. A. Huan, and L. Wang, J. Appl. Phys. **109**, 074109 (2011).
[8] D. Niermann, F. Waschkowski, J. de Groot, M. Angst, and J. Hemberger, Phys. Rev. Lett. **109**, 016405 (2012).
[9] A. Ruff, S. Krohns, F. Schrettle, V. Tsurkan, P. Lunkenheimer, and A. Lloid, Eur. Phys. J. B **85**, 290 (2012).
[10] S. Lafuerza, J. García, G. Subías, J. Blasco, K. Conder, and E. Pomjakushina, Phys. Rev. B **88**, 085130 (2013).
[11] J. de Groot, T. Mueller, R. A. Rosenberg, D. J. Keavney, Z. Islam, J.-W. Kim, and M. Angst, Phys. Rev. Lett. **108**, 187601 (2012).
[12] A. D. Christianson, M. D. Lumsden, M. Angst, Z. Yamani, W. Tian, R. Jin, E. A. Payzant, and S. E. Nagler, Phys. Rev. Lett. **100**, 107601 (2008).
[13] S. Lafuerza, G. Subías, J. Blasco, J. García, G. Nisbet, K. Conder, and E. Pomjakushina, EPL **107**, 47002 (2014).
[14] S. Lafuerza, G. Subías, J. García, J. Blasco, J. García, K. Conder, and E. Pomjakushina, Phys. Rev. B **90**, 085130 (2014).
[15] J. Blasco, S. Lafuerza, J. García, and G. Subías, Phys. Rev. B **90**, 094119 (2014).
[16] M. Inazumi, Y. Nakagawa, M. Tanaka, N. Kimizuka, and K. Siratori, J. Phys. Soc. Jpn. **50**, 438 (1981).
[17] Y. Sakai, K. Kaneda, N. Tsuda, and M. Tanaka, J. Phys. Soc. Jpn. **55**, 3181 (1986).
[18] J. García, G. Subías, M. G. Proietti, J. Blasco, H. Renevier, J. L. Hodeau, and Y. Joly, Phys. Rev. B **63**, 054110 (2001).
[19] J. A. Alonso, M. J. Martínez-Lope, M. T. Casais, M. A. G. Aranda, and M. T. Fernández-Díaz, J. Am. Chem. Soc. **121**, 4754 (1999).
[20] J. Blasco, B. Aznar, J. García, G. Subías, J. Herrero-Martín, and J. Stankiewicz, Phys. Rev. B **77**, 054107 (2008).
[21] Y. Nakagawa, M. Inazumi, N. Kimizuka, and K. Siratori, J. Phys. Soc. Jpn. **47**, 1369 (1979).
[22] S. Katano, T. Matsumoto, S. Funahashi, J. Iida, M. Tanaka, and J. W. Cable, Physica B **213-214**, 218 (1995).
[23] J. Akimitsu, Y. Inada, K. Siratori, I. Shindo, and N. Kimizuka, Solid State Commun. **32**, 1065 (1979).
[24] S. Funahashi, J. Akimitsu, Y. Inada, K. Siratori, N. Kimizuka, M. Tanaka, and H. Fujishita, J. Phys. Soc. Jpn. **53**, 2688 (1984).
[25] N. Ikeda, R. Mori, S. Mori, and K. Kohn, Ferroelectrics **286**, 175 (2003).
[26] Y. Horibe, K. Yoshii, N. Ikeda, and S. Mori, Phys. Rev. B **80**, 092104 (2009).
[27] Y. Horibe, N. Ikeda, K. Yoshii, and S. Mori, Phys. Rev. B **82**, 184119 (2010).
[28] T. Mueller, J. de Groot, J. Strempfer, and M. Angst, J. Cryst. Growth **428**, 40 (2015).
[29] N. Kimizuka and T. Katsura, J. Solid State Chem. **13**, 176 (1975).
[30] K. Kitayamo, M. Sakaguchi, Y. Takahara, H. Endo, and H. Ueki, J. Solid State Chem. **177**, 1933 (2004).
[31] F. Fauth, I. Peral, C. Popescu, M. Knapp, Powder Diffr. **28**, S360 (2013).
[32] I. Peral, J. McKinlay, M. Knapp, and S. Ferrer, J. Synchrotron Radiat. **18**, 842 (2011).
[33] J. Rodríguez-Carvajal, Physica B **192**, 55 (1993); [http://www.ill.eu/sites/fullprof/].
[34] J. M. Pérez-Mato, D. Orobengoa, and M. I. Aroyo, Acta Crystallogr. A **66**, 558 (2010).
[35] B. J. Campbell, H. T. Stokes, D. E. Tanner, and D. M. Hatch, J. Appl. Crystallogr. **39**, 607 (2006); available at ISOTROPY Software Suite, iso.byu.edu.
[36] N. E. Brese and M. O'Keeffe, Acta Crystallogr. Sect. B **47**, 192 (1991).
[37] See Supplemental Material at http://link.aps.org/supplemental/10.1103/PhysRevB.93.184110 for tables with the summary of mode decomposition and refined fractional coordinates. Figures with comparisons of x-ray patterns and refinements are also provided.
[38] K. Siratori, N. Mori, H. Takahashi, G. Oomi, I. Iida, M. Tanaka, M. Kishi, Y. Nakaawa, and N. Kimizuki, J. Phys. Soc. Jpn. **59**, 631 (1990).
[39] J. Blasco, J. García, and G. Subías, Phys. Rev. B **83**, 104105 (2011).